

Cite this: DOI: 10.1039/c0jm03842c

www.rsc.org/materials

One dimensional Si/Sn - based nanowires and nanotubes for lithium-ion energy storage materials

Nam-Soon Choi,^a Yan Yao,^b Yi Cui^{*b} and Jaephil Cho^{*a}

Received 9th November 2010, Accepted 21st December 2010

DOI: 10.1039/c0jm03842c

There has been tremendous interest in using nanomaterials for advanced Li-ion battery electrodes, particularly to increase the energy density by using high specific capacity materials. Recently, it was demonstrated that one dimensional (1D) Si/Sn nanowires (NWs) and nanotubes (NTs) have great potential to achieve high energy density as well as long cycle life for the next generation of advanced energy storage applications. In this feature article, we review recent progress on Si-based NWs and NTs as high capacity anode materials. Fundamental understanding and future challenges on one dimensional nanostructured anode are also discussed.

Introduction

In the 21st century, the era of fossil fuels such as oil will wane due to both energy and environmental concerns and the arrival of a new era of green renewable energy is expected. Solar energy, wind power, tidal power, and nuclear power are mentioned as next generation energy, but it is difficult to use these kinds of energy for transportation such as vehicles due to their uneven energy production. From this perspective, the interest in energy storage technology is on the rise as a means to solve this problem. Many batteries, such as lead–acid, nickel–cadmium, nickel–metal-hydride, zinc–bromine, zinc–air, vanadium redox, sodium–sulfur, sodium–nickel-chloride, lithium-ion, *etc.*, have been developed during past several decades.¹ It is believed that commercially available Li-ion batteries (LIBs) are the most feasible alternatives from the viewpoint of current technical maturity and economic consideration. Fig. 1a provides a comparison of energy storage devices in terms of gravimetric and volumetric energy densities, which are two key parameters for energy storage, in addition to cycle life, safety and cost.² As shown in Fig. 1a, Li-ion batteries have relatively high energy densities due to the fact that lithium is the lightest (0.53 g cm^{-3}) and most electropositive (-3.04 V vs. standard hydrogen electrode) of all the metals.² Compared to other batteries, Li-ion batteries have long cycle life, low self-discharge rate, rapid charge capability, high coulombic and energy efficiency and no memory effect.¹ The working principle of Li-ion batteries is illustrated in Fig. 1b. The positive electrode material is typically a metal oxide with layered structure (such as LiCoO_2), and the negative

electrode material is graphite. LIBs for portable electronic devices (laptops, cell phones) are attractive candidates for transportation (hybrid electric vehicles (HEVs), plug-in hybrid electric vehicles (PHEVs), electric vehicles (EVs)), bulk electricity storage at power stations and load leveling of renewable sources (solar energy and wind power). The market size of LIBs in 2020 is forecast to be around 100 billion U.S. dollars. Electrode reactions in LIBs are based on electrochemical intercalation reactions for which Li^+ ions are intercalated or deintercalated from an open host structure with a concomitant addition or removal of electrons. Although LIBs were successfully commercialized, a noticeable improvement in energy density of Li-ion cells is required to satisfy needs for high power and/or capacities for applications such as power tools, electric vehicles or efficient use of renewable energies. This can be attained by replacing the widely-used lithium cobalt oxide cathodes and carbonaceous anodes. In general, the theoretical energy density of lithium alloys is higher than those of lithiated graphite anodes (LiC_6) and metal hosts over graphite apparently do not suffer from solvent cointercalation. Despite these appreciable advantages, carbonaceous anodes are commonly used in commercial LIBs. In order to achieve lithium-ion batteries with high specific energy, some metals that can alloy lithium, such as Al, Si, Sn and Sb, have been investigated as promising negative-electrode (anode) materials. A major challenge for the implementation of alloy anodes is significant changes in structure and volume during lithium insertion and extraction, which often leads to pulverization of the active alloy particles and poor cyclability. In addition, the irreversible capacity of alloy anodes at first cycle is too high for practical applications. Extensive research has been carried out to address these two issues and discernible progress has been made.^{3–7} In particular, silicon (Si) has been extensively investigated as a promising candidate for the anode material because of its high theoretical specific capacity of 4200 mAh/g for $\text{Li}_{4.4}\text{Si}$, low electrochemical potential *versus* Li/Li^+ between 0 and 0.4 V ,

^aInterdisciplinary School of Green Energy Ulsan National Institute of Science and Technology (UNIST) 701-11, 100 Banyeon-ri, Eonyang-eup, Ulju-gun, Ulsan, Republic of Korea 689-798. E-mail: jphcho@unist.ac.kr; Fax: +82-52-217-2968; Tel: +82-52-217-2910

^bDepartment of Materials Science and Engineering, Stanford University, Stanford, California, 94305, USA. E-mail: yicui@stanford.edu

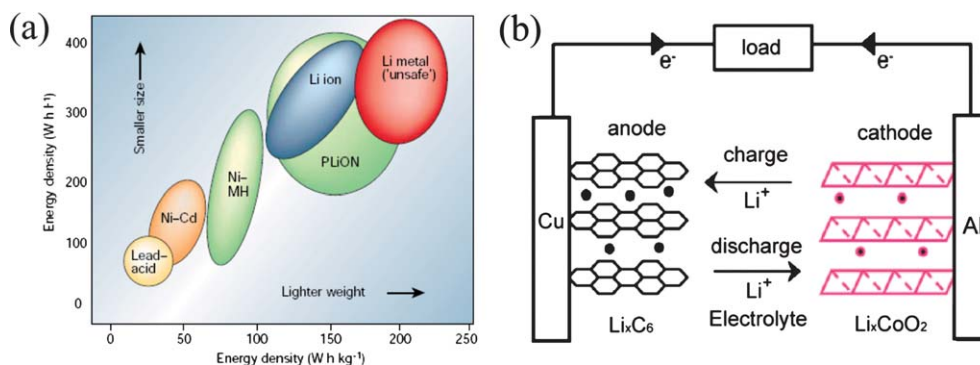


Fig. 1 (a) Comparison of a few types of batteries in terms of gravimetric and volumetric energy densities with units of Wh/kg and Wh/L, respectively. (b) Schematic diagram of a conventional lithium ion battery showing typical anode and cathode structure. During the charging process, lithium ions are de-intercalated from the cathode and intercalated into the anode.

and small initial irreversible capacity loss compared to other metal- or alloy-based anode materials.^{7–10} Si–lithium alloys do not, however, retain their high capacity on prolonged cycling. This is because large capacity fading in Si thin films¹¹ and micrometre-sized particles¹² used as electrodes in LIBs occur due to pulverization of Si and loss of electrical contact between the active material and the current collector (Fig. 2a). Various approaches have been carried out to overcome this issue, including the use of nano-sized active materials,^{10,13} active/

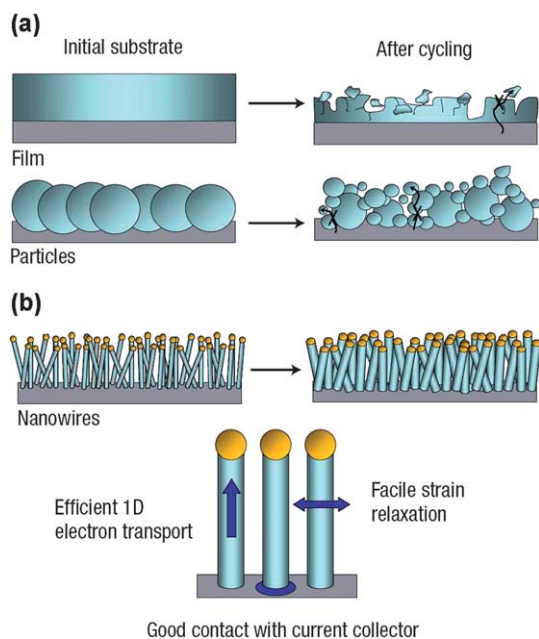


Fig. 2 Schematic of morphological changes that occur in Si during electrochemical cycling. (a) The volume of silicon anodes changes by about 400% during cycling. As a result, Si films and particles tend to pulverize during cycling. Much of the material loses contact with the current collector, resulting in poor transport of electrons, as indicated by the arrow. (b) NWs grown directly on the current collector do not pulverize or break into smaller particles after cycling. Rather, facile strain relaxation in the NWs allows them to increase in diameter and length without breaking. This NW anode design has each NW connecting with the current collector, allowing for efficient 1D electron transport down the length of every NW. Adapted with permission from ref. 49. Copyright 2008, Nature Publishing Group.

inactive composite materials,¹⁴ and silicon–carbon composites.¹⁵ The use of sub-micrometre pillars¹⁶ and microcomposite anodes¹⁷ led to limited improvement. On the other hand, the use of nanostructured materials is an effective way to improve the rate capabilities of electrodes used in batteries because of the short diffusion lengths. One dimensional (1D) nanomaterials such as nanowires and nanotubes have exhibited the enhanced electrochemical properties compared to bulk materials. This is because 1D nanomaterials allow for better accommodation of the colossal volume changes without the physical fracture that can occur in bulk or micron-sized materials. In this regard, fabrications and applications of nanostructured materials with different sizes and shapes have attracted a great deal of interest because of their different physical, chemical and photonic properties compared to bulk materials.

In this review, we focus on key aspects to apply Si, germanium (Ge), and tin (Sn)-based nanostructured materials to anode materials for LIBs. Some of the critical issues, which must be overcome for attaining high energy density and outstanding electrochemical performances of batteries containing Si/Ge/Sn nanowires or nanotubes, are discussed.

Strategies for long cycle life

Si, Sn, and Ge-based anode materials have attracted tremendous interest owing to their very high theoretical capacity (4200 mAh/g for Si ($\text{Li}_{4.4}\text{Si}$), 790 mAh/g for Sn ($\text{Li}_{4.4}\text{Sn}$), and 1600 mAh/g for Ge ($\text{Li}_{4.4}\text{Ge}$)) and are expected to significantly increase the specific energy and energy density of LIBs. Unfortunately, a large volume change of these metals during lithium insertion/extraction typically results in cracking or pulverization.^{18,19} Moreover, the resistance increases due to anisotropic volume contraction giving less effective electronic contact between metal particles during lithium extraction and, thereby, trapping of Li ions inside the host particles causing large first irreversible capacity and capacity fading takes place.¹⁷ These problems strongly limit practical applications of metals to LIBs. Among Si/Sn/Ge metals alloying with lithium, Si appears to be a promising candidate for the anode materials for LIBs due to its highest theoretical capacity.²⁰ A critical issue such as the drastic volume changes during lithium insertion/extraction resulting in disintegration of the electrodes and subsequent rapid capacity fading

remains a challenge. Exploiting nanostructured materials afford a promising means to address the challenges associated during $\text{Li}_{4.4}\text{Si}$ alloying because of the small diffusion length and facile strain relaxation during structure and volume change. In this regard, a diversity of Si structure and sizes have been contemplated including thin films,^{10,21–26} nanoparticles,^{7,27} nanowires (NWs),^{28–30} nanotubes (NTs),^{31,32} and dispersing silicon micro-particles/nanoparticles into an inactive/active matrix^{33–38} to mitigate volumetric changes of Si-based anode materials. Several methods have been examined to diminish the capacity fading of Si-based anode materials. Actually, reduction of Si particle size to nanometres is somewhat helpful to release mechanical strains within particles, decrease in lithium ion transport path length, and improve the capacity retention of Si-based anodes, but it has failed to completely exclude capacity fading. When metal nanoparticles are used as an anode material, the nanoparticles undergo aggregation and pulverization during cycling.^{39,40} More attractive strategy is to fabricate NWs and NTs that could lead to better accommodation of the large volume change during lithium insertion/extraction compared to micro- and nanoparticles. In general, the bottom-up approach starts from individual atoms or molecules to form the desired NWs. The resulting NWs display a variety of optical and magnetic properties, uniform size, and smooth surface. For nanowire synthesis based on the bottom-up approach, vapor–liquid–solid (VLS) chemical vapor deposition,^{41–45} solid–liquid–solid (SLS),^{45–47} vapor–solid (VS) reaction,²⁹ laser ablation methods,^{29,48} and a nanoporous template method have been utilized.

One of the most effective ways to prepare semiconducting Si NWs is the VLS technique. In Fig. 2b, we show that an electrode with single crystalline Si NWs grown directly on a metal current collector by VLS growth can offer several advantages. First, the small NW diameter allows for better accommodation of the large volume changes without fracture, which would typically occur in bulk or micron-sized materials. This leads to facile strain release and longer cycle life. Second, each Si NW is electrically connected to the metallic current collector so that all the NWs contribute to the capacity. Third, since Si NWs have direct 1D electronic pathways allowing for efficient charge transport, the need for binders or conducting additives is eliminated. Finally, Si NWs allow shorter Li ion diffusion distance which leads to high power density.⁴⁹

Fig. 3a and b show the SEM images of pristine Si NWs before and after electrical cycling. The Si NWs have an average diameter of ~ 89 nm (s.d. 45 nm) and length up to several tens of microns. The inset in Fig. 3a is a cross-section image showing that the NWs are directly contacting the stainless steel current collector. After charging with Li, the Si NWs had rough textured sidewalls (Fig. 3b) and the average diameter increased to ~ 141 nm (s.d. 64 nm). Despite the large volume change, the Si NWs remained intact and did not break into smaller particles. Fig. 3c shows the voltage profile of the Si NWs in a half cell, where the average charge (lithium alloying) potential is 0.15 V and the average discharge (lithium de-alloying) potential is 0.4 V. Significantly, the observed capacity during this first charging operation was 4277 mAh/g, equivalent to the theoretical capacity within experimental error. Fig. 3d shows the cycling performance of a Si NW anode at a rate of C/5 (C/5 means complete charge in 5 h). Both charge and discharge capacities were quite stable, with

a coulombic efficiency of 99% (84% in the first cycle) for about 16 cycles, after which the capacity began to drop. After 50 cycles, the capacity retention was 61%.

The local structural features of Si NWs during the first Li ion insertion were studied with transmission electron microscopy (TEM) and selected area electron diffraction (SAED). Fig. 3e shows the as-grown single crystalline Si NW with a typical $\langle 112 \rangle$ growth direction. After it was charged to 100 mV, both crystalline and amorphous phases were clearly seen in Fig. 3f. The distribution of the two phases was observed with a crystalline core and an amorphous shell. Li ions must diffuse radially into the NW from the electrolyte, resulting in the core–shell phase distribution. At 50 mV, the Si NW became mostly amorphous with some crystalline Si regions embedded inside the core, as seen from Fig. 3g. The SAED showed spotty rings representative of a polycrystalline sample and diffuse rings for the amorphous phase. At 10 mV (Fig. 3h), all of the Si had changed to amorphous $\text{Li}_{4.4}\text{Si}$, as shown by the amorphous rings in the SAED.

Si NWs for anode materials of LIBs can be also prepared by metal catalytic etching of silicon wafers^{29,44–47} and electroless etching of silicon wafers based on the top-down method.⁴⁸ Large-area, wafer-scale Si NW arrays were prepared by metal-induced chemical etching as promising scalable anode materials for rechargeable lithium batteries (Fig. 4a).²⁹ Fig. 4c shows the cross-sectional SEM image of the Si NW array after several charge/discharge cycles. The surfaces of Si NWs became much rougher after charging compared to Fig. 4b probably due to amorphization induced by the large volume change. It is clearly seen that electroless-etched Si NWs maintained structural integrity and the conducting pathway to the Si wafer for charge transport during cycling. Since the exact Si NW loading per surface area in the Si electrode was hard to estimate and the contribution of the Si wafer substrate was unknown, the contribution of the silicon wafer substrate could not be excluded from the capacity of the anode. In contrast, Zhu *et al.* reported that carbon-coated Si NW array films were prepared by metal catalytic etching of silicon wafers and pyrolyzing of carbon aerogel and the capacities of the films were from the carbon-coated Si NWs exclusively since the silicon wafer substrates were completely transformed into Si NWs.⁵⁰ It is believed that the coatings of carbon enhance the electrochemical performances. Indeed the rapid capacity fading of the uncoated Si NW film electrode was shown after 10 cycles, while carbon-coated Si NW electrode exhibits a stable reversible capacity of 1326 mAh/g after 40 cycles (Fig. 5).

Following the VLS growth crystalline Si NW anode study, we found that Si crystalline–amorphous (c–a) core–shell NW design can result in significant improvement in power rate and cycle life.⁵¹ The schematic is shown in Fig. 6a. Amorphous silicon has superior cycling performance compared to c-Si since the volume expansion of a-Si upon lithiation is homogeneous and causes less pulverization than in the crystalline material.^{9,21} The other interesting behavior of a-Si is that it reacts with lithium at a slightly higher potential than c-Si does, which leads to the idea of using c–a core–shell Si NWs as anode materials. When limiting the charging potential, it should be possible to utilize only the amorphous shell for Li^+ storage while preserving the crystalline core as a mechanical support and efficient transport pathway.

We developed a simple method to grow c–a core–shell Si NWs without changing the growth temperature to form a crystalline/

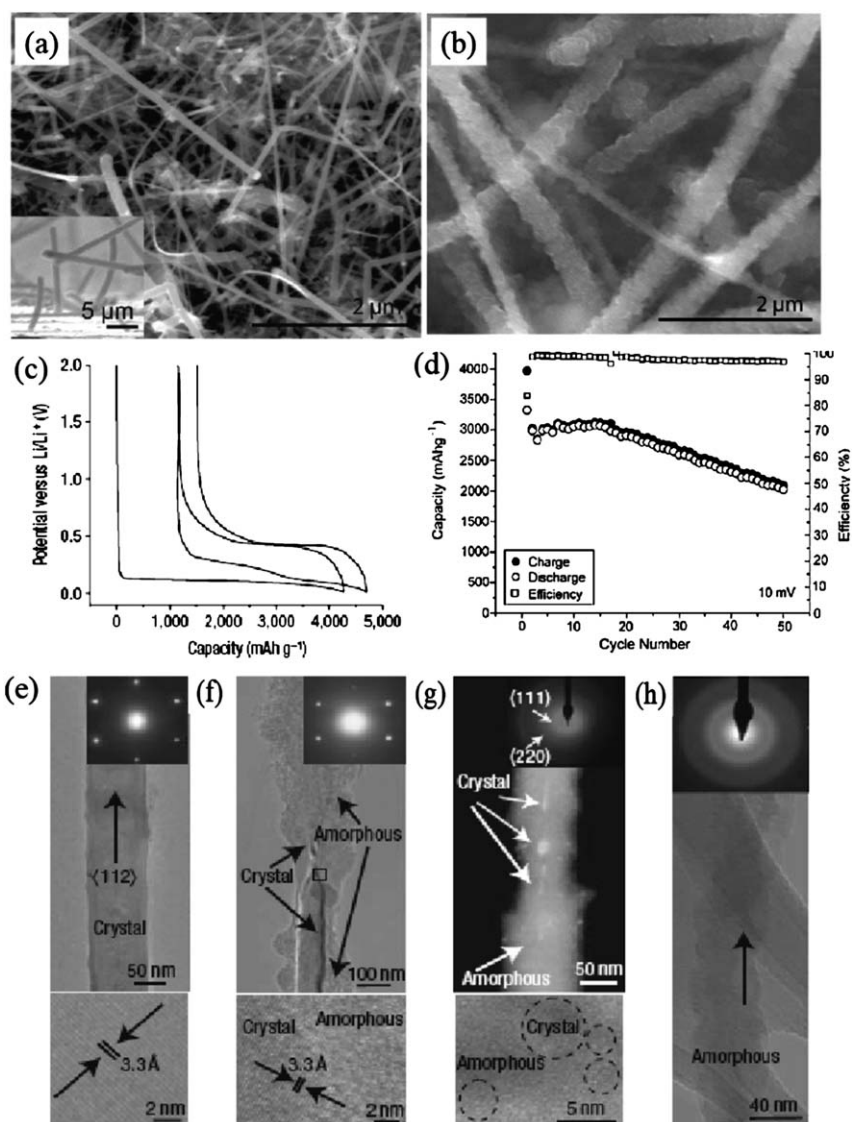


Fig. 3 SEM images of pristine Si NWs before (a) and after (b) electrochemical cycling. (c) Voltage profiles for the first and second galvanostatic cycles of the Si NWs at C/20 rate. The first charge achieved the theoretical capacity of 4200 mAh g^{-1} . (d) Cycle life of Si NWs cycled at C/5 rate with charge to 10 mV. (e) A single-crystalline, pristine Si NW before electrochemical cycling. The SAED spots and HREM lattice fringes (bottom) are from the Si $1/3(224)$ planes. (f) NW charged to 100 mV showing a Si crystalline core and the beginning of the formation of a Li_xSi amorphous shell. (g) Dark-field image of a NW charged to 50 mV showing an amorphous Li_xSi wire with crystalline Si grains (bright regions) in the core. (h) A NW charged to 10 mV is completely amorphous $\text{Li}_{4.4}\text{Si}$. The SAED (top) shows diffuse rings characteristic of an amorphous material. Adapted with permission from ref. 49. Copyright 2008, Nature Publishing Group.

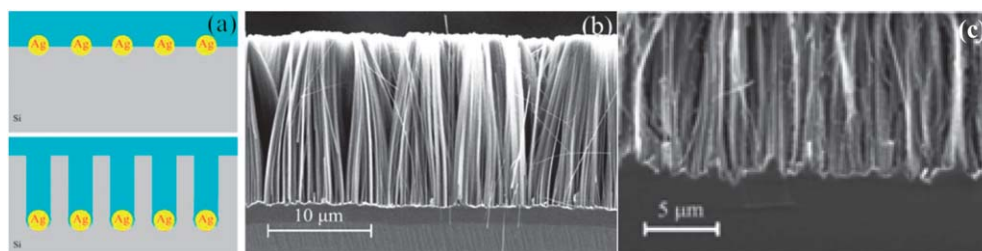


Fig. 4 (a) Schematic formation of Si nanowires *via* silver-induced etching. (b) Typical cross-sectional SEM image of Si NW arrays. (c) Typical cross-sectional SEM image of Si NW array after several charge/discharge cycles. Adapted with permission from ref. 29. Copyright 2008, American Institute of Physics publishing group.

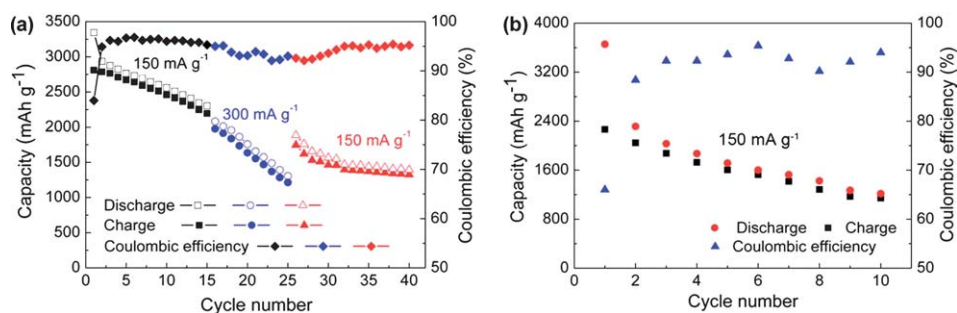


Fig. 5 (a) Capacity and coulombic efficiency of the cell based on the carbon-coated Si NW film electrode with the cycle number. (b) Capacity and coulombic efficiency of the cell containing the uncoated Si NW film electrode with the cycle number. Adapted with permission from ref. 50. Copyright 2009, American Institute of Physics publishing group.

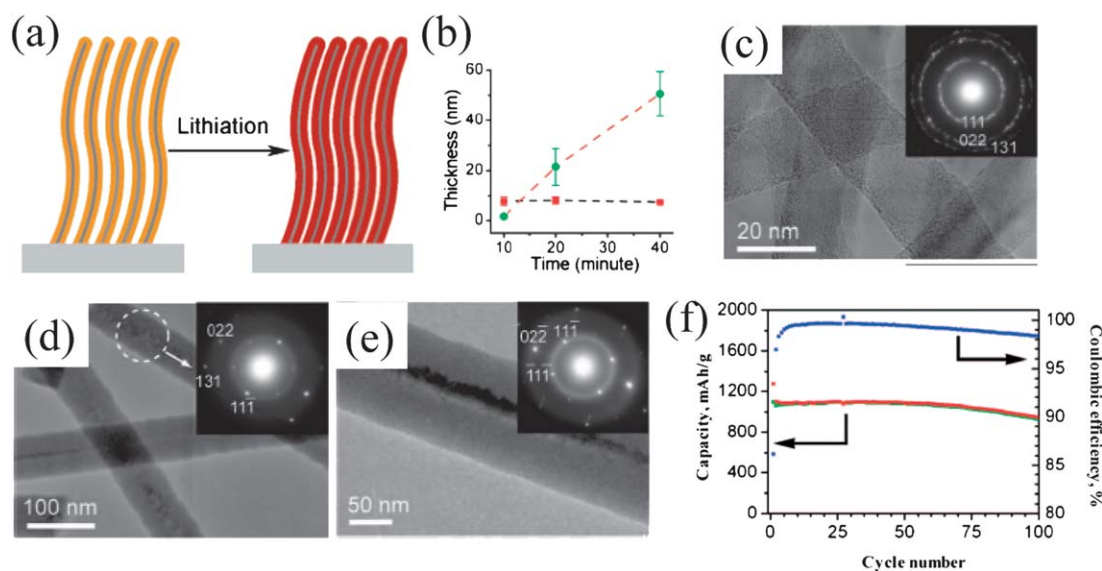


Fig. 6 (a) Schematic illustration of the lithiation of the Si c-a core-shell NWs grown on a SS substrate. (b) Statistics of the core radius (red) and shell thickness (green) versus growth time. The growth temperature was 485 °C. (c)–(e) TEM and SAED images of NWs grown for 10 min (c), 20 min (d) and 40 min (e). (f) Charge and discharge capacity and coulombic efficiency versus cycle number for the core-shell NWs with a 150 mV cut-off and at C/5. Adapted with permission from ref. 51. Copyright 2009, American Chemical Society publishing group.

amorphous region. The growth was conducted directly on stainless steel (SS) current collectors in a SiH₄ CVD furnace. Transition metals in SS, such as Ni, Fe, or Cr, are believed to catalyze the growth by a direct vapor–solid growth since Fe and Ni have been shown to catalyze this kind of growth.⁵² Fig. 6(b) shows the statistics of the core radius and shell thickness versus growth time. Fig. 6(c)–(e) shows the TEM images and SAED patterns of Si NWs grown for different growth times. For 10 min of growth, the NWs are mostly single crystalline (Fig. 6c) with little amorphous shell. For 20 min, a thick layer of amorphous shell is observed (Fig. 6d), which becomes even thicker for a 40 min growth (Fig. 6e). As shown in Fig. 6b, the thickness of the shell increased linearly with growth time while the core radius remained constant.

To confirm that the core-shell structure is robust enough for mechanical and electrical support after cycling, we investigated the morphology and structure of NWs after cycles with SEM and TEM. Two samples cycled at either 10 or 150 mV cutoffs are compared. When a 10 mV cutoff was used, the whole NW would react with lithium to go through the c-a phase transformation

repeatedly and fatigue would occur. In contrast, c-a core-shell NWs with a 150 mV cutoff and the same current density show dramatic improvement of cycle life. The c-a NW electrode was charged to 150 mV in 1.2 h, showing a capacity of ~1060 mAh g⁻¹. After 15 cycles using a 150 mV cutoff, the NWs still maintain a distinct wire shape.

The ability to synthesize Si NWs on a large scale would enable dramatic cost reduction compared to the VLS method. To this end, Si NWs were grown by a supercritical fluid–liquid–solid (SFLS) technique developed by Korgel's group at large scale (>45 mg h⁻¹).⁵³ Fig. 7a shows the majority of SFLS Si NWs with an average diameter of 24.6 nm and a length of >10 μm.²⁸ The as-grown Si NWs were single crystalline, but often had a thin coating of polyphenylsilanes which are formed as a reaction byproduct during the SFLS growth.

The slurry method is used to coat Si NWs onto current collectors. In the traditional slurry coating process, the active material is mixed with a conducting additive and a binder, suspended into a slurry, and coated onto a current collector as a composite. One major problem for the slurry method is the loss

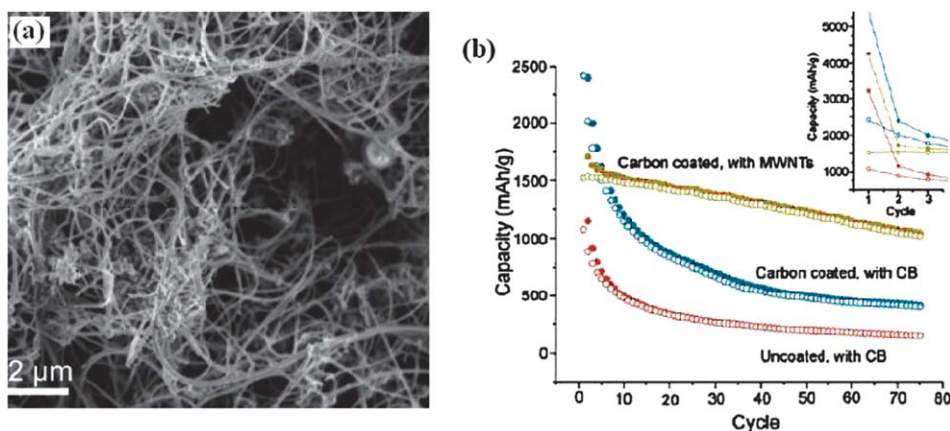


Fig. 7 (a) SEM images of SFLS Si NWs as grown. (b) Capacity vs. cycling data for SFLS Si NWs uncoated and mixed with carbon black, carbon-coated and mixed with carbon black, and carbon-coated and mixed with multiwalled carbon nanotubes with an additional nanotube overcoat layer. The data for first three cycles are shown in the inset. Adapted with permission from ref. 55. Copyright 2000, Science publishing group.

of electrical contact between Si and conducting additives during volume expansion and contraction. We investigated carboxymethyl cellulose (CMC) as the binder as well as multiwalled carbon nanotubes (MWNTs) as the conductive additives. Fig. 8b shows capacity *versus* cycling data for SFLS Si NWs with different surface coating and conductive additive. The uncoated sample consisted of pristine Si NWs mixed with carbon black and CMC at a weight ratio of 78 : 12 : 10. This electrode performed poorly with an irreversible capacity loss of 66% in the first cycle and rapid capacity loss. The carbon coated by sucrose on a Si NW sample mixed with carbon black and CMC at a weight ratio of 65 : 9 : 8 (with carbon coating for 18 wt%) also displayed a high irreversible capacity loss of 55% and fast degradation, slightly higher than those without carbon coating. A sample containing carbon-coated Si NWs with MWNTs and CMC was found to display even higher capacities due to improved

electronic conductivity of MWNT network and resiliency of the electrode to buffer the large volume changes.

In order to fabricate Si tubular nanostructures, arrays of dense ZnO nanorods as a sacrificial template were first grown using a hydrothermal process,⁵⁴ and then chemical vapor deposition (CVD) of Si onto these nanorods was performed. Lastly, ZnO was selectively removed *via* a high temperature reduction process.⁵⁵ Although large volume changes occur, the Si NTs retain their shapes with a modest increase of about 50% (120 to 180 nm) in diameter at a fully lithiated state. Subsequently, after full delithiation, this diameter is reduced from 180 to 140 nm corresponding to an increase of 17% compared to that of the pristine Si NT (Fig. 8a and b). The inset of Fig. 8d indicates that the Si transforms into an amorphous phase after one cycle, consistent with the previous report.⁵⁶ Fig. 8c presents cross sectional images of the same samples in Fig. 8a. It is found that there is no delamination of the Si NT from the stainless steel substrate with cycling (Fig. 8c), consistent with good cycle retention properties. The first full lithiation leads to volumetric expansion of the Si NTs in which the lengths undergo small increases (~5%) while the diameter increases by nearly 150%. It should be noted that reversible behavior of an electrode is critically important for reliable operation.^{57,58}

In order to determine whether the Si NT morphology is changed after cycling, the cells were disassembled and the anode was further characterized. Fig. 9a shows an SEM image of the electrode after 200 cycles; its original morphology is apparently retained. In addition to these structural changes, Fig. 9a shows that the morphology of the NTs did not change after cycling. The initial pore wall thickness of the Si NTs is ~40 nm, and no pulverization occurred even though the thickness expanded to ~300 nm. Simple mechanical mixing of the electroactive metals generally leads to an inhomogeneous mixture actually resulting in greater capacity fading than chemical homogenization.^{59,60}

Besides Si-based nanostructured anode materials, one-dimensional SnO₂ NW has also attracted much attention because of its unique properties such as a wide band gap ($E_g = 3.6$ eV at 300 K) for applications from electronic devices to gas sensors.^{61–63} Moreover, SnO₂-based materials have been suggested as one of the most promising candidates for anode materials in terms of

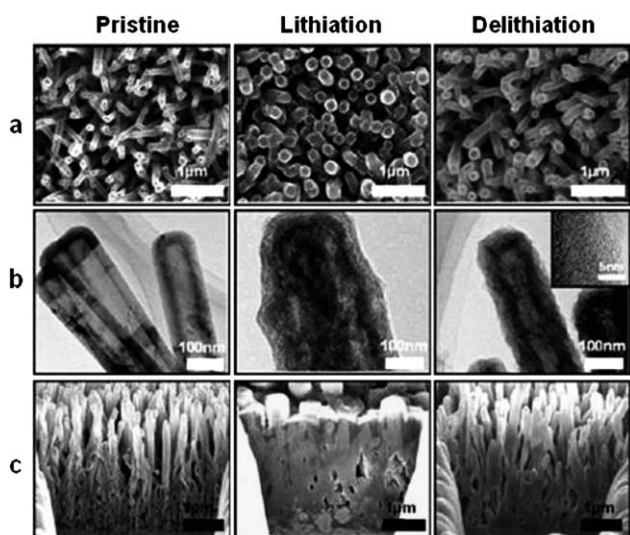


Fig. 8 Electron microscopy images of Si NTs before reaction and after full lithiation and delithiation. (a) Top view SEM images, (b) TEM images, (c) Cross-sectional SEM images of Si NTs. Adapted with permission from ref. 32. Copyright 2010, American Chemical Society publishing group.

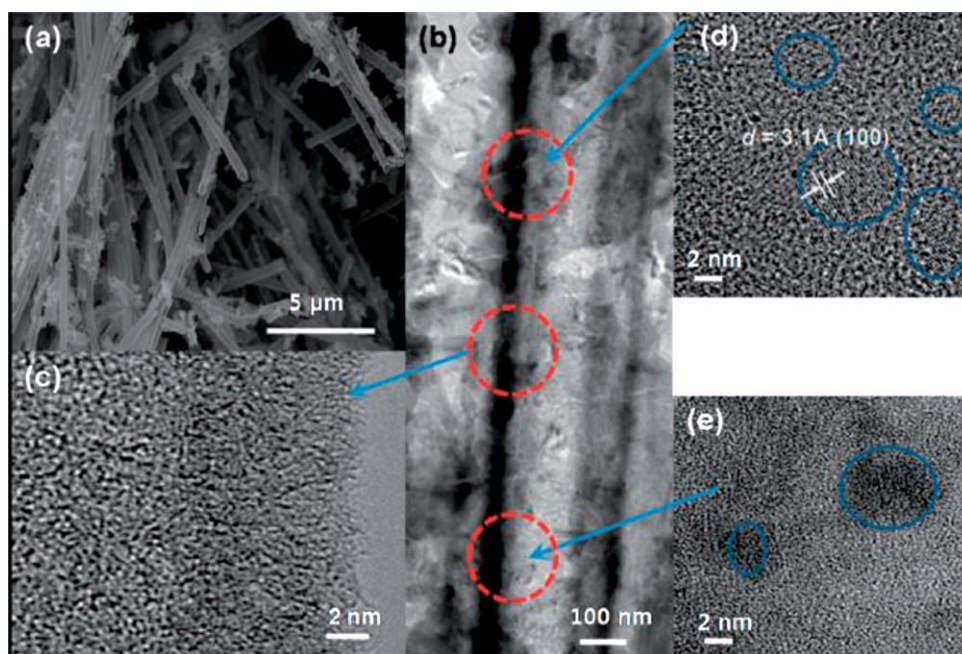


Fig. 9 (a) SEM image of cycled Si NTs (Si NTs were extracted from the Li-ion cell after 200 cycles). (b) TEM image of (a). (c, d, and e) HREM images of dotted red circles in (b). Blue circles indicate the nanocrystalline domains. Adapted with permission from ref. 31. Copyright 2009, American Chemical Society publishing group.

their high theoretical capacity of 790 mAh/g according to the following reactions: $\text{SnO}_2 + 4\text{Li}^+ + 4\text{e}^- \rightarrow \text{Sn} + 2\text{Li}_2\text{O}$, $\text{Sn} + x\text{Li}^+ + xe^- \rightarrow \text{Li}_x\text{Sn}$ ($0 \leq x \leq 4.4$).⁶⁴ However, Li_2O formation and volume expansion of the Sn phase during Li insertion are the main barriers that cannot be applied to LIBs as anode materials. The Li_2O phase provokes the large initial irreversible capacity and the significant capacity fading of Sn-based anodes during cycling. It should be noted that the use of nanostructured materials could lead to the decomposition of the undesirable Li_2O phase and the suppression of the volume expansion of the Sn phase.^{60,63,65} In order to realize tubular 1D nanomaterials, anodic aluminium oxide (AAO) and polycarbonate (PC) membrane-template methods have been widely used.^{56,57,66} In particular, the tubular SnO_2 prepared by a template-assisted method using AAO exhibits a significant improvement of electrochemical performance over the unorganized nanoparticles.⁵⁸ The cyclability of the NTs and their primitive nanoparticles are compared in Fig. 10c. The specific capacity of the unorganized SnO_2 is drastically reduced from 676 mAh/g to 65 mAh/g after 80 cycles. It is well known that the fast capacity fading with SnO_2 nanoparticles is ascribed to an asymmetrical volume change of aggregated nanoparticles (Fig. 10a). Compared to the unorganized SnO_2 , the SnO_2 NT electrode showed superior specific discharge capacity of 940 mAh/g during the first cycle and the degree of capacity fading was smaller. The specific capacity of the Sn-based NT electrode was 525 mAh/g after 80 cycles (Fig. 10c). Even if the SnO_2 nanoparticles possess high surface area, they tend to aggregate due to their high mobility.⁶¹

Recently, our group reported nanoscale coating of an Si layer on the pore walls of SnO_2 NTs (Si-coated SnO_2), which led to very good electrochemical performance in coulombic efficiency, rate capability and capacity retention compared with untreated SnO_2 NTs.⁶² SnO_2 from SnCl_4 hydrolysis was first deposited on

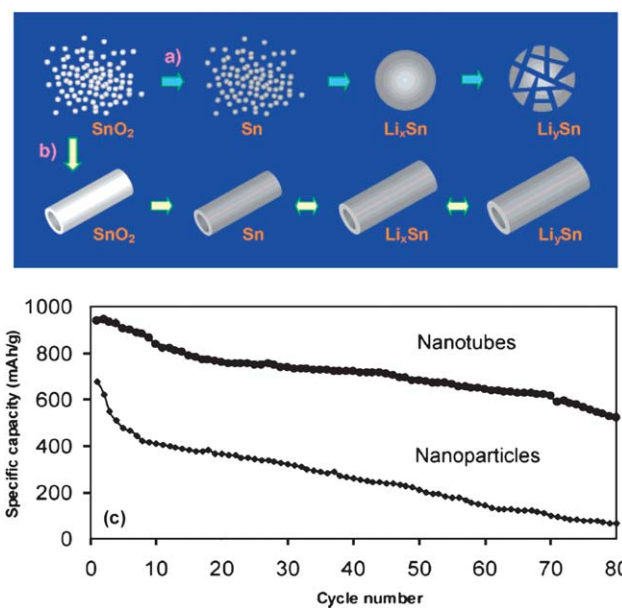


Fig. 10 Schematic illustrations of SnO_2 in two different fabrications. (a) Aggregations of resultant Sn (or Li_xSn) and pulverization of Li_ySn (assuming $y \gg x$) occur upon lithiation and delithiation. (b) When nanocrystallites of SnO_2 are organized into a tubular configuration, concentric expansion and contraction could be expected upon lithium charging and discharging. (c) Cyclabilities of SnO_2 nanotube electrodes and SnO_2 nanoparticle electrodes (5 mV to 2 V, 0.05 mA cm⁻²; voltage versus Li^+/Li). Adapted with permission from ref. 58. Copyright 2005, American Chemical Society publishing group.

the inside pore walls of an alumina membrane followed by coating the SnO_2 with butyl-capped Si gels. Subsequent thermal annealing at 1000 °C for 3 h in Ar converted the butyl moieties to

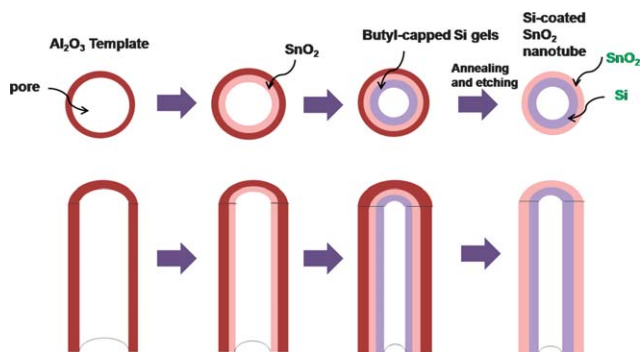


Fig. 11 Schematic diagrams for the preparation procedure of Si-coated SnO₂ NTs. Adapted with permission from ref. 62. Copyright 2010, The Royal Society of Chemistry.

amorphous carbon on Si. The alumina membrane was then removed by NaOH etching to recover the Si-coated SnO₂ NTs (Fig. 11). Fig. 12f compares the reversibility of Li ion storage in Si-coated SnO₂ NTs and in SnO₂ and Si NTs in coin-type half cell measurements between 0 and 1.2 V. The first cycle discharge (lithium extraction) capacity and coulombic efficiency of the Si-coated SnO₂ NTs were 1838 mAh/g and 65%, respectively, considerably higher than the corresponding values for SnO₂ NTs (960 mAh/g and 47%). On the other hand, the first charge and discharge capacities of the Si nanoparticles prepared by butyl-capped Si gels were 3980 and 3535 mAh/g, respectively. The considerable capacity fading of the SnO₂ NTs is attributed to anisotropic volume expansion and contraction causing the mechanical pulverization of nanotubes under internal stress. Substantial fragmentation of the tubular SnO₂ NT electrode was observed after 90 cycles (Fig. 12e). In the Si-coated NTs, however, capacity fading was moderated by the amorphous Si layer, which buffered the inward volume expansion of the SnO₂ NTs rather well. On the other hand, there was no way to buffer the volume expansion outwards of the tube wall. This is why the Si-coated SnO₂ NTs still exhibited some deterioration of the

tube wall structure along the length of the tube (Fig. 12a and b). However, the overall tubular morphology was mostly retained compared to SnO₂ NTs.

Ge is also one of the promising candidates because of its high theoretical capacity (*ca.* 1600 mAh/g) and faster Li diffusivity than Si. Moreover, the Ge NWs exhibit better capacity retention at higher C rates compared to Si NWs. In this regard, simple thermal annealing of the Sn₇₈Ge₂₂ nanoparticles capped with alkyl groups has been observed to turn them into branched NWs.⁶³ Using butyl-capped Sn₇₈Ge₂₂ nanoparticles, vacuum-annealing of these 0D nanoparticles could lead to the formation of Sn₇₈Ge₂₂@carbon core/shell NWs.^{8,60,63,64}

Fig. 13b exhibits a transmission electron microscopy (TEM) image of butyl-capped Sn₇₈Ge₂₂ nanoparticles before annealing. It is found that approximately 1 μm sized particles are connected to each other. After the sample was thermally vacuum-annealed at 600 °C, the morphology completely changes to branched NWs with diameters in the range of 50–100 nm and lengths of several micrometres. Specific capacity of the NWs at 1C rate is 1054 mAh/g and the capacity retention at 8C is about 88% (Fig. 13f). This impressive electrochemical performance is attributed to the morphology and the presence of the carbon shell that inhibit aggregation into larger particles. This result is in good agreement with the previous study that the electrochemical stability of Si nanoparticles could be improved by encapsulation in a porous carbon matrix to form Si–C nanocomposites.^{67–73} The other important phenomenon for Si nanostructure anodes, particularly Si NWs, is the porous structure formation. In the charging process, Si can take up about 4.4 Li per Si, and its volume upon full lithiation is even larger, up to 400% of the original. As Li is extracted in the discharging process, the expanded active materials shrink, but the final volume at the end of the discharging is still larger than the original, which indicates the formation of void space inside the active materials. Thus, the pore formation depends directly on the volumetric expansion of the active materials in the charging process and the atomic diffusion of the active materials in the discharging process. When the atomic

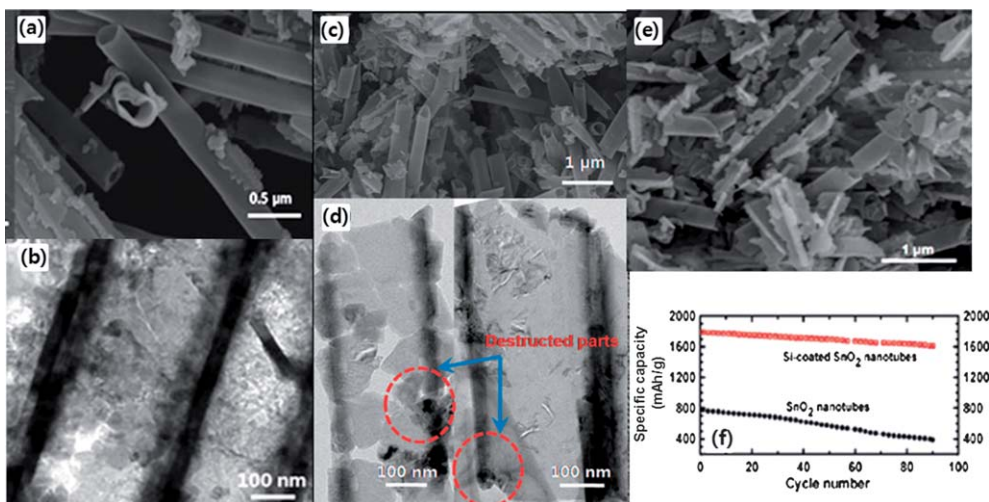


Fig. 12 SEM (a, c) and TEM (b, d) images of Si-coated SnO₂ before and after cycling. (e) SEM images of SnO₂ NTs after cycling for 90 times at a rate of 0.5C. (f) Specific capacity vs. cycle number of Si-coated SnO₂ NTs at the 0.5C rate in coin-type half cells. Adapted with permission from ref. 62. Copyright 2010, The Royal Society of Chemistry.

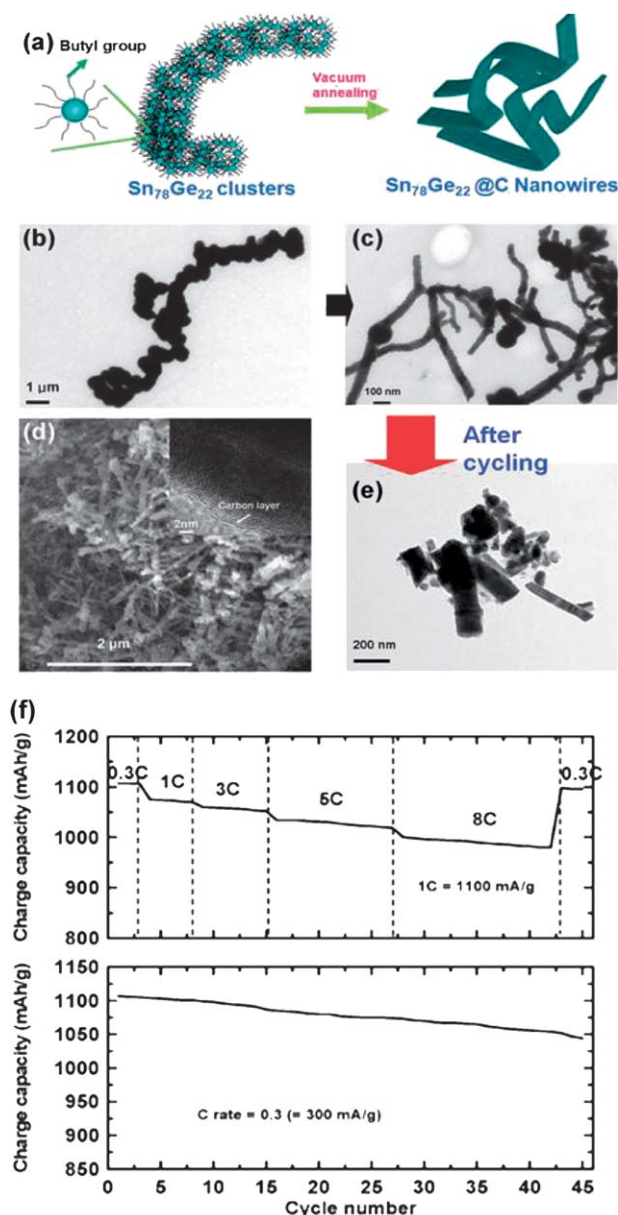


Fig. 13 (a) Schematic view of the preparation of the Sn₇₈Ge₂₂@carbon core/shell NWs from butyl-capped Sn₇₈Ge₂₂ clusters. (b, c) TEM images of the Sn₇₈Ge₂₂@carbon core/shell NWs before and after annealing. (d) SEM image of the Sn₇₈Ge₂₂@carbon core/shell NWs (the inset is a TEM image of the edge part of the NWs). (e) TEM image of the NWs after cycling. (f) Rate capabilities and cycle life performance of the coin-type half cells. Adapted with permission from ref. 63. Copyright 2007, American Chemical Society publishing group.

diffusion of active materials is slow during the discharging process, the active materials tend to form pores more efficiently because the slow diffusion prohibits the active materials from returning to their original structures. Instead, thermodynamically metastable structures with pores generated inside are preferred. We studied the stepwise pore evolution of Si NWs.⁷⁴ During the lithiation–delithiation processing, Si NWs become more and more porous, as illustrated in Fig. 14a. In the alloying–dealloying processing, we found that the pore sizes are tunable by the number of cycles. As shown in Fig. 14b, the nanopore sizes

increase with cycling, indicated by BET (Brunauer–Emmett–Teller) measurements. This observation is reflected in the pore size increases in the pore size distribution. Fig. 14c and d show the SEM images of Si NWs after 5 and 10 cycles in the discharged state. The smooth Si NWs become completely porous with large diameter increases. It is likely that some Si material comes off the Si NWs. The porous structure of such Si NWs has been proposed and tested for double layer supercapacitor applications.

High mass loading of nanostructured Si materials

Although current collectors take up more weight than active materials in most lithium ion battery cells, so far research has been focused mainly on improving gravimetric capacities of active materials. The ideal current collector should minimize its own weight. We exploited carbon nanotube (CNT) and carbon nanofiber (CNF) networks to function as both mechanical support and electrical conductors.^{75,76} Assuming that these free-standing platforms are used in commercial 18650 cells whose typical areal capacities are $\sim 4 \text{ mA cm}^{-2}$, $\sim 23\%$ mass reduction is expected on the anode side.

To demonstrate the bifunctionality of the designed structure as both current collector and active anode material, a free-standing CNT-Si film was fabricated by chemical vapor deposition of amorphous Si onto CNT film. Fig. 15a shows a photograph of a free-standing CNT-Si composite film, which is highly conductive, $\sim 30 \text{ ohm sq}^{-1}$ sheet resistance, and flexible. Fig. 15b shows the cycling performance of a 4 μm thick CNT-Si film at a rate of 0.1C. The discharge capacity is 2083 mAh g⁻¹ at the beginning and remains at 1711 mAh g⁻¹ (or 82%) after 50 cycles. The coulombic efficiency is 86% for the first cycle and greater than 98% throughout the remaining cycles.

In order to deposit crystalline Si NWs on the carbon network, a layer of gold was first thermally deposited as a catalyst for VLS growth. After the CVD growth, the original black CNF film changed to a brown CNF-Si NW nanocomposite (Fig. 15d) and Si NWs firmly bind onto CNF films. This unique feature allows Si NWs to remain well-bound during cycling and thus achieve a good cycle life. As shown in Fig. 15e, Si NWs are mainly on the surface where gold layers were deposited, but some Si NWs penetrate into CNF films because gold catalyst layers are broken into nanoparticles and the nanoparticles diffuse into the CNF layers during the VLS growth. The areal capacity remains above 5 mAh cm⁻² for a sample with a 3.6 mg cm⁻² mass loading. Similar overall nanocomposite thicknesses ($\sim 20 \text{ μm}$) before and after cycling confirm the robust mechanical properties of the nanocomposite.

In addition, we have demonstrated that theoretical charge capacity was achieved for crystalline Si NWs grown by CVD.⁴⁹ However, the mass loading is relatively low ($\sim 0.3 \text{ mg cm}^{-2}$), which corresponds to an areal capacity of $\sim 1 \text{ mAh cm}^{-2}$, lower than the commercial value of 4 mAh cm⁻². Longer growth time could increase the mass loading, while making the cost prohibitively high. Here we show two solutions to effectively increase mass loading to the commercial mass loading scale. The first solution was sketched in Fig. 16a and b as a design of carbon–silicon core–shell NWs by CVD of amorphous Si onto carbon nanofibers (CNFs).⁷⁷ Due to CNFs' small capacity, it has little volume change with charge potential down to 10 mV versus

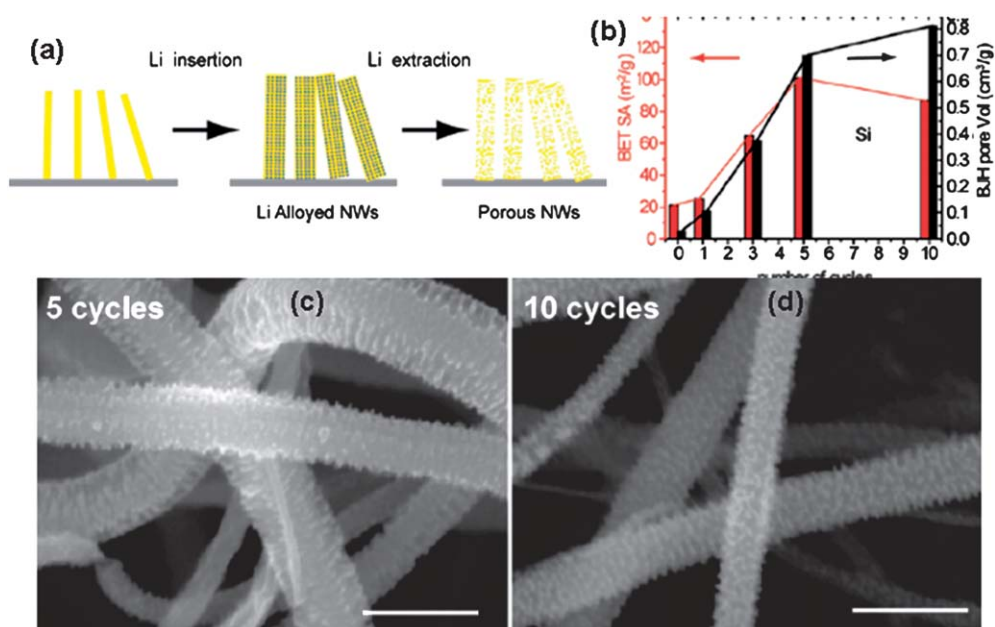


Fig. 14 (a) Schematic illustration of pore generation by the alloying/dealloying process. As-grown silicon nanowires expand upon electrochemical Li ion insertion. As Li ions are extracted from these 1D nanomaterials, the nanostructures shrink but to volumes larger than the original. The increased volumes suggest pore formation inside the nanostructures. (b) The BET surface area and pore volume changes for different numbers of Li-battery cycles. The increase in pore volume is more abrupt than the increase in BET surface area. Very small pore volumes at 0 Li-battery cycles indicate that interwire spacing is negligible in our measurement range (<300 nm) for both materials. (c, d) SEM images of Si NWs after 5 and 10 Li-battery cycles. All the scale bars are 200 nm. Adapted with permission from ref. 74. Copyright 2010, American Chemical Society publishing group.

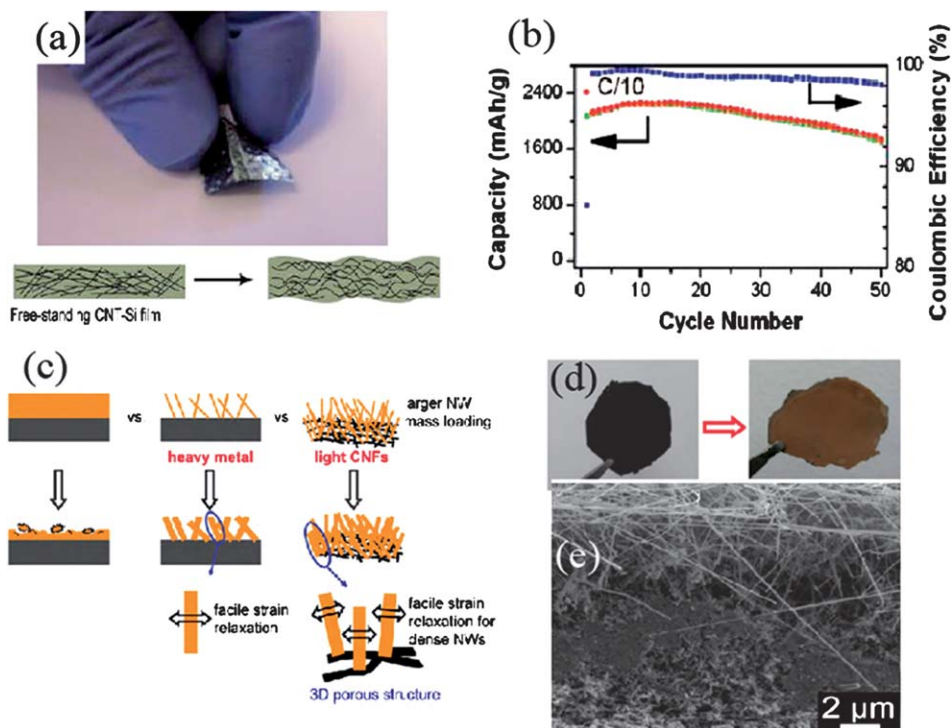


Fig. 15 (a) Photograph of a free-standing CNT-Si film and schematic showing CNT-Si films can “ripple up” to release large strain during Li⁺ ion intercalation. (b) Charge (red) and discharge (green) capacity and coulombic efficiency (blue) versus cycle number for a half cell using single layer free-standing CNT-Si films as the working electrode cycled between 1 and 0.01 V. (c) Schematic comparison of a Si layer on a flat metal current collector to Si NWs on a light CNF film before cycling. The 3D porous structure of the CNF film facilitates a larger number of Si NWs compared to Si NWs on the flat substrate. (d) Photographs of a freestanding CNF film before and after CVD growth. (e) A cross-section SEM of a CNF-Si NW nanocomposite. Adapted with permission from ref. 75. Copyright 2010, American Chemical Society publishing group.

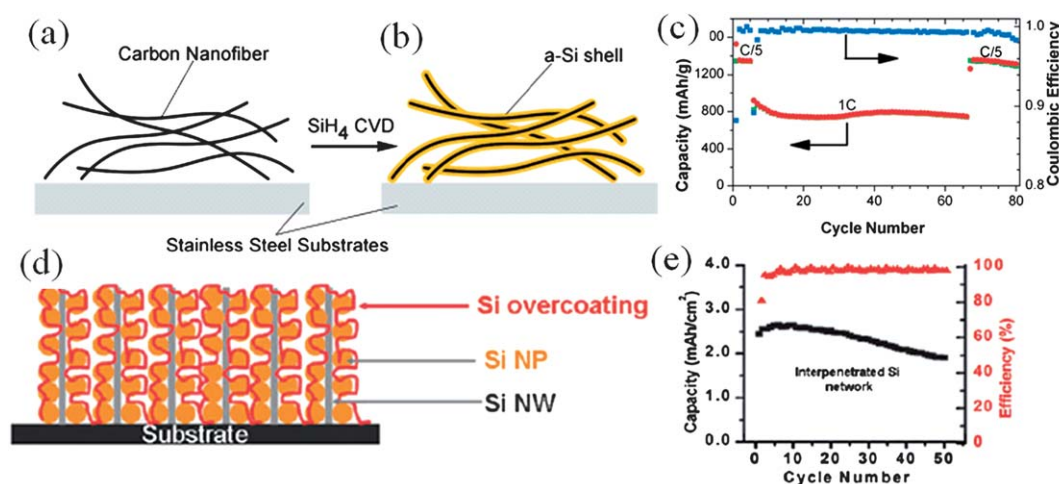


Fig. 16 Schematic illustration of Si coating onto carbon nanofibers. (a) Bare CNFs. (b) Carbon–Si core–shell NWs. (c) Charge and discharge capacity and coulombic efficiency *versus* cycle number for a half cell cycled between 1 and 0.1 V at high rate. (d) Schematic of Si nanoparticle (NP)-decorated Si NWs. The Si nanoparticles are drop-cast directly onto CVD-grown Si NW networks to increase the mass loading of active materials. (e) Areal capacity of the Si nanoparticle-Si NW network anode and its coulombic efficiency. Adapted with permission from ref. 77. Copyright 2009, American Chemical Society publishing group.

lithium metal. In addition, CNFs are commercially available in a large quantity. CVD temperature was set at 500 °C, slightly higher than the crystalline-Si deposition temperature, and the pressure was set between 10 and 30 Torr. Small silane flow and lower pressure produce better conformal coating of Si onto CNFs. The mass loading of Si was $\sim 1.2 \text{ mg cm}^{-2}$. At the rate of 0.2C (1C = 2.5 Ag^{-1}), a reversible capacity of $\sim 2000 \text{ mA g}^{-1}$ was observed for the first 30 cycles. After the first cycle, the cell maintained a very high coulombic efficiency between 98–99.5% for the remaining cycles. In Fig. 16c, the half cell was tested at 1C between 1–0.1 V. The capacity remains at a large value of 800 mAh g^{-1} . After a total of 80 cycles, the discharge capacity showed very little decay ($\sim 7\%$) compared to the first cycle discharge capacity.

The other solution to increase mass loading is to use Si nanoparticles to decorate Si NWs (Fig. 16d). This design has several advantages as a high energy density anode: first, the commercial Si nanoparticles ($\sim 50 \text{ nm}$ diameter) can effectively increase the mass loading of Si NW electrodes. The low viscosity of the Si ink allows for easy penetration of Si nanoparticles into the Si NW network. Second, Si NWs function as both active electrode and electrical pathways to the current collector for the Si nanoparticles. To physically fix Si nanoparticles onto Si NWs and to improve charge transport, a layer of amorphous Si coating by CVD can function as the conducting path. Third, the nanoporous 3D structure provides enough space for the expansion of both Si NWs and Si nanoparticles.

The total mass of Si effectively increases from 0.3 mg cm^{-2} to 1.5 mg cm^{-2} . The binder-free network allows for a high mass loading per volume compared to the traditional slurry-based structure in which conductive super-P was used as additive particles. Fig. 16e show the coulombic efficiency and cycling performance of the Si nanoparticle decorated network. The areal capacities for the Si NW anode increase from $\sim 0.6 \text{ mA h cm}^{-2}$ to $\sim 2.5 \text{ mA h cm}^{-2}$ for the decorated Si network, a roughly 4-fold improvement.

Mechanical modeling of Si NWs during lithiation

Mechanical modeling is important to gain a full picture of the mechanical properties of Si anodes during lithiation and delithiation. Wang *et al.* conducted a theoretical *ab initio* modeling of single Li atom insertion into Si NWs with different size and axis orientations.⁷⁸ They found that different types of Si NWs will introduce different binding energies, among which the binding energy of [110] Si NWs become bulk-like the fastest. Li has the highest diffusivity in the [110] direction because Si presents open hexagonal ion channels in this direction. Qi *et al.* computed the elastic properties of Si dependence on Li ion concentration using DFT calculation.⁷⁹ Fig. 17a shows the Young's modulus significantly decreases in the Li-rich phases. The modulus of Li–Si alloys drops by about an order of magnitude compared to its original value of Si when it is fully lithiated. This elastic softening can be explained by considering the charge-density and atomic bonding in lithiated alloys.

Sethuraman *et al.* did experimental measurements (*in situ*) of stress evolution in silicon thin films during lithiation and delithiation.⁸⁰ A multi-beam optical sensor (MOS) technique is used for measuring stress evolution, shown in Fig. 17b. MOS is insensitive to vibrations, which makes it useful for thin film stress monitoring in a variety of problems.^{81,82} The relationship between the biaxial film stress and the substrate curvature is given by the Stoney equation. Fig. 17c and d show the cell potential and the film stress plotted against the capacity of the silicon thin-film electrode. It is interesting to see that upon lithiation compressive stress builds up and increases linearly with time. Assuming the strain induced by Li in Si is proportional to its concentration, the linear increase in the compressive stress indicates an elastic response. The film seems to reach the elastic limit at a compressive stress of about 1.7 GPa, and begins to show plastic flow with further lithiation in order to accommodate additional volume expansion. Upon delithiation, the unloading is initially elastic; the stress reverses elastically until it becomes

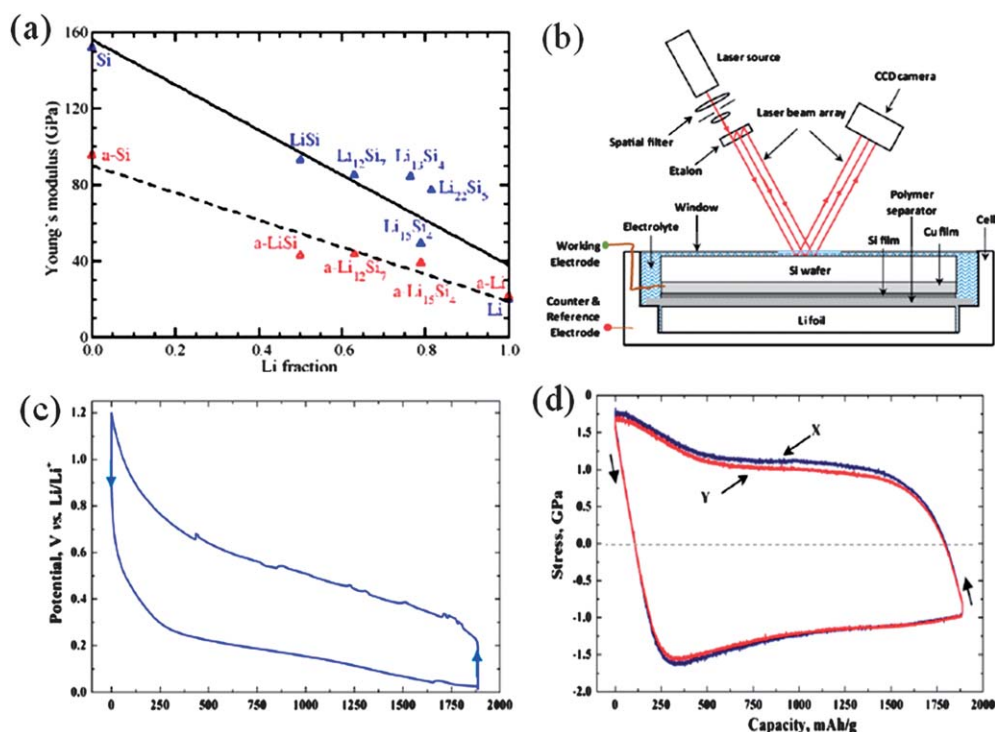


Fig. 17 (a) Young's modulus of Li–Si alloys plotted as a function of Li fraction in crystalline (solid symbols) and in amorphous (open symbols) phases for the alloy Li_xSi . Solid and broken lines show linear fits for the crystalline and the amorphous systems, respectively. (b) Schematic of an electrochemical-cell assembly and a MOS setup to measure substrate curvature. (c) Cell potential vs. capacity curve corresponding to the lithiation and delithiation of Si thin-film electrode cycled at C/4 rate between 1.2 and 0.01 V vs. Li/Li^+ . (d) Corresponding stress calculated from the substrate curvature data using the Stoney equation. Adapted with permission from ref. 80. Copyright 2010, Elsevier publishing group.

about 1 GPa in tension, where the film begins to flow in tension in order to accommodate the reduction in volume. The flow stress increases to about 175 GPa when the upper potential limit of 1.2 V is reached.

Solid electrolyte interface (SEI) on Si-based anodes

As mentioned before, the use of appropriate voids (or space) in NWs and NTs capable of accommodating the significant volume changes allows better capacity retention during cycling. Even though nanostructured materials such as NWs and NTs are promising configurations, high reversible capacity and a stable cycle life cannot be feasible without good electrical contacts between anode materials and interfacial stability toward electrolyte components. Earlier studies on Si thin film electrodes revealed that decreasing the thickness of the Si film leads to good electrical contacts and thus stable electrochemical performances irrespective of crack formation.^{9,25}

Here, we report alluring ways to stabilize the interface between Si-based anode materials and electrolytes. First, coating with carbon on the surface of a nanostructured Si electrode can accommodate the dramatic volume expansion while maintaining better the electrically conductive network and preventing the breakdown of the SEI layer. Crack formation during repeated charge–discharge cycling results in the exposure of new surfaces to the electrolyte and a continuous SEI-filming process sacrificing the reversible capacity.^{19,83} Second, functional additives can be used to form a stable SEI layer contributing to the

reduction of reversible capacity and better cycling performances. The property of SEI determines the coulombic efficiency of initial cycles as well as the long term stability of the electrode material.^{84–86}

In recent work,⁸⁷ a better fundamental understanding of the morphological changes of Si NTs during cycling was achieved. Si NTs with a rigid nano- confined space using a carbon NTs (CNTs) outer shell were fabricated by the following procedure: alumina membranes with ~ 300 nm pores were coated with (a) ~ 40 nm of C via C_3H_6 decomposition at 700°C at 1 atm pressure, (b) Si via SiH_4 decomposition at 500°C , and (c) ~ 5 nm of C and etched in a HF solution. The resulting membranes, consisting of nearly identical vertical tubes (Fig. 18a), were mechanically and electrically connected to the Cu foil current collector using a PVDF binder (Fig. 18b). No increase in Si tube length after cycling was observed and the compressed Si tubes were typically attached to one of the CNT walls, providing electrical contact. The evidence for contraction and partial delamination of the inner Si tube from the CNT surface after the Li extraction is clearly shown in Fig. 18c and d. Multiple cracks previously seen in planar thin Si films were not observed in tubular samples and there were no major defects in the carbon walls after cycling. The produced Si nanotubes with a rigid C outer shell showed high capacity and stable electrochemical performance. In addition, the size-preserving external rigid carbon shell enables a very high coulombic efficiency ($>99\%$) and the formation of a stable SEI layer, which serves as a barrier to electrolyte decomposition. The CNT walls were demonstrated to

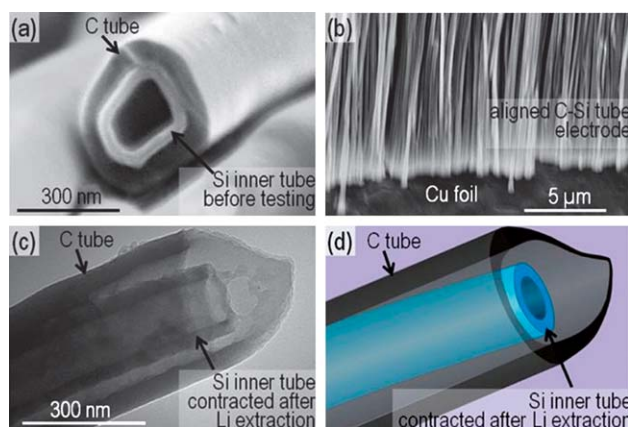


Fig. 18 Electron microscopy of the composite Si tube with a rigid C outer shell. (a) SEM of the synthesized samples, (b) SEM of the electrode attached to a Cu current collector, (c) TEM and (d) its schematic illustration of a Si inner tube inside a C tube after Li extraction at the 10th cycle. Adapted with permission from ref. 87. Copyright 2010, American Chemical Society publishing group.

be capable of withstanding internal stresses caused by the initial Si expansion during Li intercalation. It can be considered that these findings provide prospective guidance for the efficient design of viable nanostructured Si anodes.

In a similar manner, a coating approach with carbon was carried out to form composites of SnO₂ and carbon at the nanoscale that aim to attain the high capacity of SnO₂ and the good cyclability of carbon.

Fig. 19 presents carbon nanotube (CNT)-encapsulated SnO₂ nanotubes fabricated *via* a nanoporous template method.⁸⁸ The CNT-encapsulated SnO₂ nanotubes were fabricated by treating SnO₂ nanotubes with CVD of CNTs. The SnO₂-filled alumina templates serve as the starting material for the fabrication of SnO₂-core/carbon-shell tubular nanostructures. CVD treatment of the SnO₂ nanotubes in an AAO membrane using acetylene as the carbon source led to the encapsulation of the SnO₂ nanotubes by a thin layer of CNTs. The CNT shell provides good electrical contact and could accommodate the reaction-induced stress by using the space in the open tubular structure for free material expansion. This SnO₂/C composite nanostructure showed excellent cycling behavior (Fig. 19). These outstanding electrochemical performances are probably linked to tubular organization of tin-oxide nanoparticles, stress absorption by the CNT matrix, and the presence of a hollow interior allowing freedom of

expansion, increased electrical contact, and enhanced lithium-ion transport.

Maier *et al.* pointed out the importance of SEI film former in Si@SiO_x/C nanocomposite electrodes.⁷³ It is well known that use of electrolyte additives is one of the most effective ways for improving electrochemical performances of Li-ion batteries. Much effort has been devoted to the formation of an electrochemically stable surface layer between the carbon-based anode and the electrolyte solution.^{89–97} Unfortunately, there are few works on interfacial properties of metal alloy anodes such as Si and Sn with electrolytes. For the silicon anode system, there have been several studies focused on the SEI formation of amorphous Si thin films and particles.⁹⁸ The characteristics of the surface layer formed on the Si-based anode represent a key parameter that influences the kinetics of lithiation–delithiation and the interfacial stability during long-term cycling. The formation of the surface layer is attributed to the electrochemical reduction of the organic solvents and salts. Moreover, its morphology and composition strongly depend on the electrolyte components.^{99–101} The electrolyte that is commonly used in commercial LIBs is lithium hexafluorophosphate (LiPF₆) in a mixture of organic solvents. The PF₆[−] anion undergoes an equilibrium, *i.e.*, LiPF₆ (sol.) ↔ LiF (s) + PF₅ (sol.), in solvents. The strong Lewis acid PF₅ tends to react with organic solvents and labile P–F bonds are highly susceptible to hydrolysis even if trace amounts of moisture are present in the electrolyte solution,^{102,103} *i.e.*, LiPF₆ (sol.) + H₂O → POF₃ (sol.) + LiF (s) + 2HF (sol.) and PF₅ (sol.) + H₂O → POF₃ (sol.) + 2HF (sol.). The resulting HF reacts with the Si phase and thereby leads to the formation of cracks in the Si–Si network, *i.e.*, Si + 4HF + 2F[−] + 2h⁺ → SiF₆^{2−} + 2H⁺ + H₂ (g).¹⁰⁴ This means that Si-based active materials become electrochemically inactive and thereby the capacity utilization in LiPF₆-based electrolyte significantly decreases. It was reported that an attempt was made to stabilize the interface between a Si thin-film electrode and the electrolyte solution through the use of vinylene carbonate and fluoroethylene carbonate as electrolyte additives.^{8,19} We found that the surface layer at the interface between the Si thin film anode and the electrolyte without FEC additive contains metastable linear alkyl carbonates (–Si–OCH₂CH₂O–CO₂Li, –Si–CH₂CH₂OCO₂Li, R(OCO₂Li)₂). These compounds with –Si–C– (bonding energy = 318 kJ mol^{−1}) and –Si–O– (452 kJ mol^{−1}) moieties can be electrochemically broken resulting in the continuous decomposition of electrolytes due to the low bonding energy. In contrast, it was clearly seen that the SEI layer consists mainly of stable LiF and compounds with –Si–F

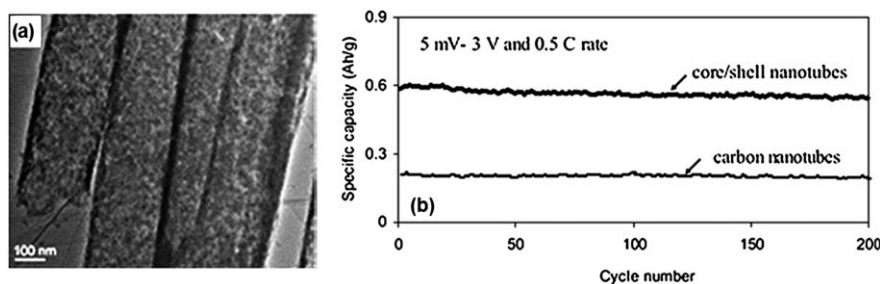


Fig. 19 (a) TEM image of a few oriented SnO₂-core/carbon-shell nanotubes. (b) Cycling performance of SnO₂-core/carbon-shell nanotubes and CNTs. Adapted with permission from ref. 88. Copyright 2006, WILEY-VCH Verlag GmbH & Co. KGaA publishing group.

(565 kJ mol⁻¹) moieties. These compounds do not tend to decompose owing to their high bonding energy and can retain the stable interface on the prolonged cycling.

In the case of the Si NW anode, we studied the SEI formation using X-ray photoelectron spectroscopy (XPS) and electrochemical impedance spectroscopy (EIS).¹⁰⁵ Because of their large surface areas, the Si NWs are expected to have a higher reactivity with the electrolyte, which implies that the SEI formation can affect the long term cycling performance of the cell significantly. XPS gives surface information based on the elemental and bonding analysis on the Si NWs. Fig. 20a and b show the composition and the molecular species of the surface at different potentials, respectively. During the first lithiation cycle, the SEI grows so thick that the silicon signal disappears. The composition varies during cycling; however, two molecular species—lithium fluoride (LiF) and lithium carbonate (Li₂CO₃)—are the major components during complete charge–discharge cycles. Although this inorganic SEI is stable and insoluble regardless of the potential, the organic components of the SEI, such as PEO-containing oligomers, are rather unstable and soluble depending on the potential range.

The long term stability of an electrode requires a stable SEI layer. The way to form a stable SEI layer on Si NWs remains an open question. There are some promising approaches, such as using electrolyte additives to *in situ* form a stable layer or pre-coating a thin artificial SEI layer on Si NWs.

In addition, it is clearly demonstrated that electrolyte additives can improve the electrochemical performance of Si@SiO_x/C nanocomposite as a promising anode of LIBs.⁷³ When vinylene carbonate (VC) as a stable SEI former is added to the electrolyte,^{106,107} the Si nanoparticles show a slightly better cycling performance compared to the VC-free electrolyte. The Si@SiO_x/C nanocomposite shows better cycling performance than the pure Si nanoparticles, but it still exhibits drastic capacity fading in the VC-free electrolyte (Fig. 21). This indicates that the SiO_x/C coating on Si nanoparticles is not sufficient for achieving good cycling performance. Surprisingly, an excellent cycling performance was achieved in VC-containing electrolyte. This result coincides with the previous works on improving electrochemical performance of Si-based anode materials using SEI forming additives.^{8,19} The initial irreversible capacity loss mainly originated from the trapping of Li in host active materials and the

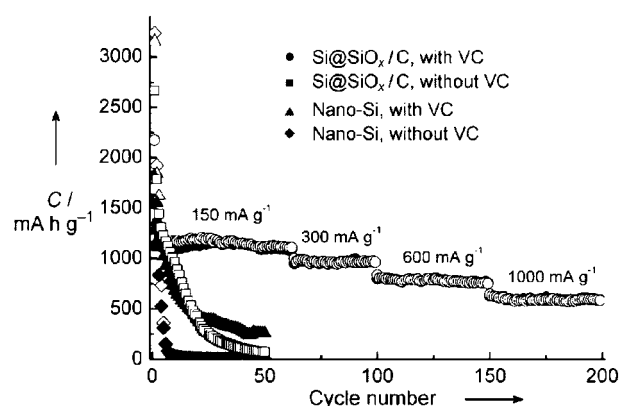


Fig. 21 Cycling and rate performance of pure Si nanoparticles and Si@SiO_x/C nanocomposite electrodes cycled in VC-free and VC-containing 1 M LiPF₆ in EC/DMC solutions (solid symbols: charge; empty symbols: discharge). Adapted with permission from ref. 73. Copyright 2008, WILEY-VCH Verlag GmbH & Co. KGaA publishing group.

reductive decomposition of the electrolyte was observed. This critical issue can be overcome by performing an artificial SEI layer on the active particles and/or prelithiating the active particles.¹⁰⁸ It is obvious that building innovative electrolyte additives is an immediate technological solution for LIBs based on nanostructured anode materials.

Conclusions

We demonstrated the key research that is necessary for the development of practical Si/Sn anodes for Li-ion batteries with high energy density.

1. One dimensional nanostructured materials such as NTs and NWs exhibited a significant improvement of electrochemical performance due to the short diffusion lengths and better accommodation of large volume changes.
2. Quantitative measurements of the dimensional changes of Si NTs and mechanical modeling of Si NWs provided the fundamental understanding of their morphology and stress changes upon lithiation and delithiation.
3. Feasible solutions for high mass loading to apply nanostructured materials to practical Li-ion battery anodes were

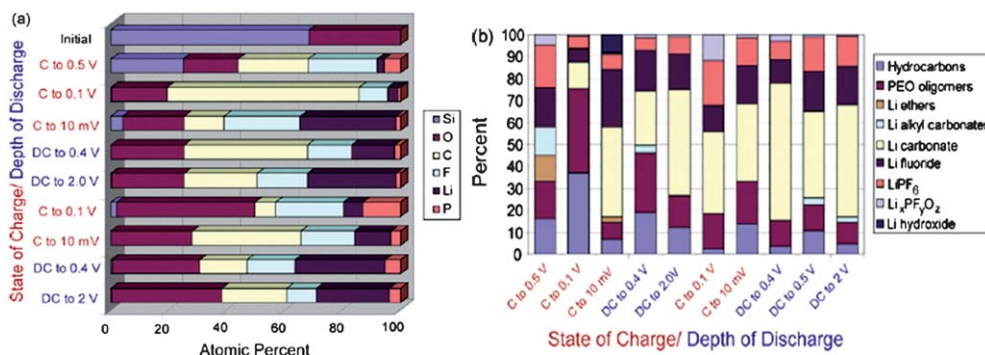


Fig. 20 (a) Surface composition and (b) molecular species of Si NW samples at different potentials as derived from the XPS scan. The atomic percentages are shown for different potentials during the charge and discharge. Adapted with permission from ref. 105. Copyright 2009, Elsevier publishing group.

offered using carbon–silicon core–shell NWs and Si nanoparticles to decorate Si NWs. Moreover, carbon nanotube (CNT) and carbon nanofiber (CNF) networks could be exploited instead of using heavy metal current collectors.

4. Using electrolyte additives for build-up of a thin and stable artificial SEI layer could assure the long term stability of Si-based anodes. In addition, the existence of an exterior carbon shell allowing freedom of expansion retained electrical contact and served as a barrier to further electrolyte decomposition.

It is believed that the present results and associated analysis provide more general design guidelines for advanced nanostructures with the promise of further improvement in electrochemical performances.

Acknowledgements

This work was supported by the Converging Research Center Program through the Ministry of Education, Science and Technology (2010K000984) and by the IT R&D program of MKE/IITA (Core Lithium Secondary Battery Anode Materials for Next Generation Mobile Power Module, KI001784). Yi Cui, Y. Yao acknowledge the support from the King Abdullah University of Science and Technology (KAUST) Investigator Award (No. KUS-11-001-12).

References

- D. Linden and T. B. Reddy, *Handbook of Batteries*, 2002.
- J. M. Tarascon and M. Armand, *Nature*, 2001, **414**, 359–367.
- J. Yang, Y. Takeda, N. Imanishi and O. Yamamoto, *J. Electrochem. Soc.*, 1999, **146**, 4009–4013.
- Y. Liu, K. Hanai, K. Horikawa, N. Imanishi, A. Hirano and Y. Takeda, *Mater. Chem. Phys.*, 2005, **89**, 80–84.
- W. R. Liu, Z. Z. Guo, W. S. Young, D. T. Shieh, H. C. Wu, M. H. Yang and N. L. Wu, *J. Power Sources*, 2005, **140**, 139–144.
- Z. P. Guo, J. Z. Wang, H. K. Liu and S. X. Dou, *J. Power Sources*, 2005, **146**, 448–451.
- H. Li, X. J. Huang, L. Q. Chen, Z. G. Wu and Y. Liang, *Electrochem. Solid-State Lett.*, 1999, **2**, 547–549.
- L. B. Chen, K. Wang, X. H. Xie and J. Y. Xie, *J. Power Sources*, 2007, **174**, 538–543.
- J. P. Maranchi, A. F. Hepp and P. N. Kumta, *Electrochem. Solid-State Lett.*, 2003, **6**, A198–A201.
- U. Kasavajjula, C. S. Wang and A. J. Appleby, *J. Power Sources*, 2007, **163**, 1003–1039.
- T. D. Hatchard, M. N. Obrovac and J. R. Dahn, *J. Electrochem. Soc.*, 2006, **153**, A282–A287.
- C. M. Park and H. J. Sohn, *Electrochim. Acta*, 2009, **54**, 6367–6373.
- H. Li, X. J. Huang, L. Q. Chen, G. W. Zhou, Z. Zhang, D. P. Yu, Y. J. Mo and N. Pei, *Solid State Ionics*, 2000, **135**, 181–191.
- O. Mao, R. L. Turner, I. A. Courtney, B. D. Fredericksen, M. I. Buckett, L. J. Krause and J. R. Dahn, *Electrochem. Solid-State Lett.*, 1999, **2**, 3–5.
- J. Yang, B. F. Wang, K. Wang, Y. Liu, J. Y. Xie and Z. S. Wen, *Electrochem. Solid-State Lett.*, 2003, **6**, A154–A156.
- M. Green, E. Fielder, B. Scrosati, M. Wachtler and J. S. Moreno, *Electrochem. Solid-State Lett.*, 2003, **6**, A75–A79.
- J. H. Ryu, J. W. Kim, Y. E. Sung and S. M. Oh, *Electrochem. Solid-State Lett.*, 2004, **7**, A306–A309.
- L. Y. Beaulieu, K. W. Eberman, R. L. Turner, L. J. Krause and J. R. Dahn, *Electrochem. Solid-State Lett.*, 2001, **4**, A137–A140.
- N. S. Choi, K. H. Yew, K. Y. Lee, M. Sung, H. Kim and S. S. Kim, *J. Power Sources*, 2006, **161**, 1254–1259.
- J. Cho, *J. Mater. Chem.*, 2010, **20**, 4009–4014.
- S. Ohara, J. J. Suzuki, K. Sekine and T. Takamura, *Electrochemistry*, 2003, **71**, 1126–1128.
- H. Jung, W. L. Yoon, H. Lee, J. S. Park, J. S. Shin, H. La and J. D. Lee, *J. Power Sources*, 2003, **124**, 76–80.
- S. Ohara, J. Suzuki, K. Sekine and T. Takamura, *J. Power Sources*, 2004, **136**, 303–306.
- T. Takamura, S. Ohara, M. Uehara, J. Suzuki and K. Sekine, *J. Power Sources*, 2004, **129**, 96–100.
- J. T. Yin, M. Wada, K. Yamamoto, Y. Kitano, S. Tanase and T. Sakai, *J. Electrochem. Soc.*, 2006, **153**, A472–A477.
- D. Larcher, S. Beattie, M. Morcrette, K. Edstroem, J. C. Jumas and J. M. Tarascon, *J. Mater. Chem.*, 2007, **17**, 3759–3772.
- H. Kim, M. Seo, M. H. Park and J. Cho, *Angew. Chem., Int. Ed.*, 2010, **49**, 2146–2149.
- C. K. Chan, R. N. Patel, M. J. O'Connell, B. A. Korgel and Y. Cui, *ACS Nano*, 2010, **4**, 1443–1450.
- K. Q. Peng, J. S. Jie, W. J. Zhang and S. T. Lee, *Appl. Phys. Lett.*, 2008, **93**.
- H. Kim and J. Cho, *Nano Lett.*, 2008, **8**, 3688–3691.
- M. H. Park, M. G. Kim, J. Joo, K. Kim, J. Kim, S. Ahn, Y. Cui and J. Cho, *Nano Lett.*, 2009, **9**, 3844–3847.
- T. Song, J. L. Xia, J. H. Lee, D. H. Lee, M. S. Kwon, J. M. Choi, J. Wu, S. K. Doo, H. Chang, W. Il Park, D. S. Zang, H. Kim, Y. G. Huang, K. C. Hwang, J. A. Rogers and U. Paik, *Nano Lett.*, 2010, **10**, 1710–1716.
- J. S. Xue, K. Myrtle and J. R. Dahn, *J. Electrochem. Soc.*, 1995, **142**, 2927–2935.
- I. Kim, P. N. Kumta and G. E. Blomgren, *Electrochem. Solid-State Lett.*, 2000, **3**, 493–496.
- I. Kim, G. E. Blomgren and P. N. Kumta, *Electrochem. Solid-State Lett.*, 2003, **6**, A157–A161.
- P. Patel, I. S. Kim and P. N. Kumta, *Mater. Sci. Eng., B*, 2005, **116**, 347–352.
- Z. P. Guo, Z. W. Zhao, H. K. Liu and S. X. Dou, *J. Power Sources*, 2005, **146**, 190–194.
- A. M. Wilson, G. Zank, K. Eguchi, W. Xing and J. R. Dahn, *J. Power Sources*, 1997, **68**, 195–200.
- Y. Kim, H. Hwang, C. S. Yoon, M. G. Kim and J. Cho, *Adv. Mater.*, 2007, **19**, 92.
- G. Derrien, J. Hassoun, S. Panero and B. Scrosati, *Adv. Mater.*, 2007, **19**, 2336.
- A. I. Hochbaum, R. Fan, R. R. He and P. D. Yang, *Nano Lett.*, 2005, **5**, 457–460.
- R. S. Wagner and W. C. Ellis, *Appl. Phys. Lett.*, 1964, **4**, 89.
- F. J. Himpsel, T. Jung, A. Kirakosian, J. L. Lin, D. Y. Petrovykh, H. Rauscher and J. Viernow, *MRS Bull.*, 1999, **24**, 20–24.
- K. Q. Peng, Y. J. Yan, S. P. Gao and J. Zhu, *Adv. Mater.*, 2002, **14**, 1164–1167.
- K. Q. Peng, Y. Wu, H. Fang, X. Y. Zhong, Y. Xu and J. Zhu, *Angew. Chem., Int. Ed.*, 2005, **44**, 2737–2742.
- K. Q. Peng, J. J. Hu, Y. J. Yan, Y. Wu, H. Fang, Y. Xu, S. T. Lee and J. Zhu, *Adv. Funct. Mater.*, 2006, **16**, 387–394.
- K. Q. Peng, M. L. Zhang, A. J. Lu, N. B. Wong, R. Q. Zhang and S. T. Lee, *Appl. Phys. Lett.*, 2007, **90**.
- W. L. Xu and J. C. Flake, *J. Electrochem. Soc.*, 2010, **157**, A41–A45.
- C. K. Chan, H. L. Peng, G. Liu, K. McIlwrath, X. F. Zhang, R. A. Huggins and Y. Cui, *Nat. Nanotechnol.*, 2008, **3**, 31–35.
- R. Huang, X. Fan, W. C. Shen and J. Zhu, *Appl. Phys. Lett.*, 2009, **95**, 133119.
- L. F. Cui, R. Ruffo, C. K. Chan, H. L. Peng and Y. Cui, *Nano Lett.*, 2009, **9**, 491–495.
- Z. Q. Liu, S. S. Xie, W. Y. Zhou, L. F. Sun, Y. B. Li, D. S. Tang, X. P. Zou, C. Y. Wang and G. Wang, *J. Cryst. Growth*, 2001, **224**, 230–234.
- J. D. Holmes, K. P. Johnston, R. C. Doty and B. A. Korgel, *Science*, 2000, **287**, 1471–1473.
- L. Vayssieres, *Adv. Mater.*, 2003, **15**, 464–466.
- J. Goldberger, R. R. He, Y. F. Zhang, S. W. Lee, H. Q. Yan, H. J. Choi and P. D. Yang, *Nature*, 2003, **422**, 599–602.
- M. Lahav, T. Sehayek, A. Vaskevich and I. Rubinstein, *Angew. Chem., Int. Ed.*, 2003, **42**, 5575–5579.
- M. Steinhart, R. B. Wehrspohn, U. Gosele and J. H. Wendorff, *Angew. Chem., Int. Ed.*, 2004, **43**, 1334–1344.
- Y. Wang, J. Y. Lee and H. C. Zeng, *Chem. Mater.*, 2005, **17**, 3899–3903.
- M. N. Obrovac and L. Christensen, *Electrochem. Solid-State Lett.*, 2004, **7**, A93–A96.
- M. G. Kim and J. Cho, *J. Electrochem. Soc.*, 2009, **156**, A277–A282.

- 61 J. J. Zhu, Z. H. Lu, S. T. Aruna, D. Aurbach and A. Gedanken, *Chem. Mater.*, 2000, **12**, 2557–2566.
- 62 W. J. Lee, M. H. Park, Y. Wang, J. Y. Lee and J. Cho, *Chem. Commun.*, 2010, **46**, 622–624.
- 63 H. Lee and J. Cho, *Nano Lett.*, 2007, **7**, 2638–2641.
- 64 J. Graetz, C. C. Ahn, R. Yazami and B. Fultz, *J. Electrochem. Soc.*, 2004, **151**, A698–A702.
- 65 C. K. Chan, X. F. Zhang and Y. Cui, *Nano Lett.*, 2008, **8**, 307–309.
- 66 J. Chen, Z. L. Tao and S. L. Li, *J. Am. Chem. Soc.*, 2004, **126**, 3060–3061.
- 67 G. X. Wang, J. H. Ahn, J. Yao, S. Bewlay and H. K. Liu, *Electrochem. Commun.*, 2004, **6**, 689–692.
- 68 T. Hasegawa, S. R. Mukai, Y. Shirato and H. Tamon, *Carbon*, 2004, **42**, 2573–2579.
- 69 X. L. Yang, Z. Y. Wen, X. J. Zhu and S. H. Huang, *Electrochem. Solid-State Lett.*, 2005, **8**, A481–A483.
- 70 S. H. Ng, J. Z. Wang, D. Wexler, K. Konstantinov, Z. P. Guo and H. K. Liu, *Angew. Chem., Int. Ed.*, 2006, **45**, 6896–6899.
- 71 W. Wang and P. N. Kumta, *J. Power Sources*, 2007, **172**, 650–658.
- 72 Y. S. Jung, K. T. Lee and S. M. Oh, *Electrochim. Acta*, 2007, **52**, 7061–7067.
- 73 Y. S. Hu, R. Demir-Cakan, M. M. Titirici, J. O. Muller, R. Schlogl, M. Antonietti and J. Maier, *Angew. Chem., Int. Ed.*, 2008, **47**, 1645–1649.
- 74 J. W. Choi, J. McDonough, S. Jeong, J. S. Yoo, C. K. Chan and Y. Cui, *Nano Lett.*, 2010, **10**, 1409–1413.
- 75 L. F. Cui, L. B. Hu, J. W. Choi and Y. Cui, *ACS Nano*, 2010, **4**, 3671–3678.
- 76 J. W. Choi, L. B. Hu, L. F. Cui, J. R. McDonough and Y. Cui, *J. Power Sources*, 2010, **195**, 8311–8316.
- 77 L. F. Cui, Y. Yang, C. M. Hsu and Y. Cui, *Nano Lett.*, 2009, **9**, 3370–3374.
- 78 Q. F. Zhang, W. X. Zhang, W. H. Wan, Y. Cui and E. G. Wang, *Nano Lett.*, 2010, **10**, 3243–3249.
- 79 V. B. Shenoy, P. Johari and Y. Qi, *J. Power Sources*, 2010, **195**, 6825–6830.
- 80 V. A. Sethuraman, M. J. Chon, M. Shimshak, V. Srinivasan and P. R. Guduru, *J. Power Sources*, 2010, **195**, 5062–5066.
- 81 J. A. Floro, E. Chason, S. R. Lee, R. D. Twisten, R. Q. Hwang and L. B. Freund, *J. Electron. Mater.*, 1997, **26**, 969–979.
- 82 E. Chason and B. W. Sheldon, *Surf. Eng.*, 2003, **19**, 387–391.
- 83 M. Winter and J. O. Besenhard, *Electrochim. Acta*, 1999, **45**, 31–50.
- 84 E. Peled, *J. Electrochem. Soc.*, 1979, **126**, 2047–2051.
- 85 D. Aurbach, B. Markovsky, M. D. Levi, E. Levi, A. Schechter, M. Moshkovich and Y. Cohen, *J. Power Sources*, 1999, **81–82**, 95–111.
- 86 J. S. Gnanaraj, R. W. Thompson, J. F. DiCarlo and K. M. Abraham, *J. Electrochem. Soc.*, 2007, **154**, A185–A191.
- 87 B. Hertzberg, A. Alexeev and G. Yushin, *J. Am. Chem. Soc.*, 2010, **132**, 8548–8549.
- 88 H. C. Z. a. J. Y. L. Y. Wang, *Adv. Mater.*, 2006, **18**, 645–649.
- 89 D. Bar-Tow, E. Peled and L. Burstein, *J. Electrochem. Soc.*, 1999, **146**, 824–832.
- 90 E. Peled, D. B. Tow, A. Merson, A. Gladkikh, L. Burstein and D. Golodnitsky, *J. Power Sources*, 2001, **97–98**, 52–57.
- 91 E. Peled, C. Menachem, D. BarTow and A. Melman, *J. Electrochem. Soc.*, 1996, **143**, L4–L7.
- 92 C. Menachem, E. Peled, L. Burstein and Y. Rosenberg, *J. Power Sources*, 1997, **68**, 277–282.
- 93 Y. EinEli and V. R. Koch, *J. Electrochem. Soc.*, 1997, **144**, 2968–2973.
- 94 Y. P. Wu, C. Jiang, C. Wan and R. Holze, *J. Power Sources*, 2002, **111**, 329–334.
- 95 Y. L. Cao, L. F. Xiao, X. P. Ai and H. X. Yang, *Electrochem. Solid-State Lett.*, 2003, **6**, A30–A33.
- 96 Q. M. Pan, K. K. Guo, L. Z. Wang and S. B. Fang, *J. Electrochem. Soc.*, 2002, **149**, A1218–A1223.
- 97 Q. M. Pan, K. K. Guo, L. Z. Wang and S. B. Fangz, *Electrochem. Solid-State Lett.*, 2003, **6**, A265–A267.
- 98 D. K. Kim, P. Muralidharan, H. W. Lee, R. Ruffo, Y. Yang, C. K. Chan, H. Peng, R. A. Huggins and Y. Cui, *Nano Lett.*, 2008, **8**, 3948–3952.
- 99 H. Ota, Y. Sakata, A. Inoue and S. Yamaguchi, *J. Electrochem. Soc.*, 2004, **151**, A1659–A1669.
- 100 R. Mogi, M. Inaba, S. K. Jeong, Y. Iriyama, T. Abe and Z. Ogumi, *J. Electrochem. Soc.*, 2002, **149**, A1578–A1583.
- 101 K. C. Moller, H. J. Santner, W. Kern, S. Yamaguchi, J. O. Besenhard and M. Winter, *J. Power Sources*, 2003, **119–121**, 561–566.
- 102 K. Xu, *Chem. Rev.*, 2004, **104**, 4303–4417.
- 103 K. Xu, S. S. Zhang, T. R. Jow, W. Xu and C. A. Angell, *Electrochem. Solid-State Lett.*, 2002, **5**, A26–A29.
- 104 N. S. Choi, K. H. Yew, H. Kim, S. S. Kim and W. U. Choi, *J. Power Sources*, 2007, **172**, 404–409.
- 105 C. K. Chan, R. Ruffo, S. S. Hong and Y. Cui, *J. Power Sources*, 2009, **189**, 1132–1140.
- 106 M. Holzapfel, H. Buqa, F. Krumeich, P. Novak, F. M. Petrat and C. Veit, *Electrochem. Solid-State Lett.*, 2005, **8**, A516–A520.
- 107 M. Holzapfel, H. Buqa, W. Scheifele, P. Novak and F. M. Petrat, *Chem. Commun.*, 2005, 1566–1568.
- 108 Q. M. Pan, H. B. Wang and Y. H. Jiang, *Electrochem. Commun.*, 2007, **9**, 754–760.